PAPER • OPEN ACCESS

First of its kind: a test artifact for direct laser writing

View the article online for updates and enhancements.

First of its kind: a test artifact for direct laser writing

Sven Fritzsche* , **Brian R Pauw** , **Christiane Weimann and Heinz Sturm**[1]

Bundesanstalt für Materialforschung und -prüfung, Unter den Eichen 87, 12205 Berlin, Germany

E-mail: sven.fritzsche@bam.de

CrossMark

Abstract

With femtosecond-laser direct writing (fs-LDW) maturing in all aspects as a manufacturing technology, a toolset for quality assurance must be developed. In this work we introduce a first of its kind test artifact. Test artifacts are standardized 3D models with specific geometric features to evaluate the performance of writing parameters. Test artifacts are already common in other 3D additive manufacturing technologies e.g. selective laser melting. The test artifact introduced in this work was developed in particular to accommodate (1) the high geometrical resolution of fs-LDW structures and (2) the limited possibilities to examine the resulting structure. Geometric accuracy, surface adhesion as well as confocal Raman spectroscopy results were considered when evaluating the design of the test artifact. We will explain the individual features and design considerations of our fs-LDW test artifact. The difference between two slicers, Cura and 3DPoli, and the implications on measured feature sizes and the general shape is quantified. The measured geometries are used to derive a general design guide for a specific combination of photoresists, laser power and scanning speed and to analyze the geometric accuracy of a structure produced using these guidelines. The shown test artifact is publicly available as STL file on GitHub (https://github.com/BAMresearch/2PP-TestArtifact) and in the supplement.

Supplementary material for this article is available online

Keywords: test artifact, two photon polymerization, direct laser writing, quality infrastructure, multi photon lithography, laser direct writing

(Some figures may appear in colour only in the online journal)

1. Introduction

Laser Direct Writing (LDW) via two-photon polymerization (2PP) or multi-photon lithography (MPL) has matured towards a versatile manufacturing technology. The fabricated objects range from a few micrometers [1] to centimeters in size. The feature size of these objects can be in the sub-micron range depending on multiple parameters. [2] Only with a coordinated orchestration of positioning tables, optical components and the appropriate control parameters, as well as suitable control software, can an exact replica with the desired properties be fabricated. A wide range of different applications would benefit from the use of test artifacts biomedical applications [3–5], optical elements [6–8] or microfluidic [9, 10] objects fabricated in-place as well as reference structures for roughness measurements [11, 12]. Indeed, these processes also need to be adapted to the materials used, such as hybrid polymers [13], biocompatible hydrogels [14–16], ceramics [17, 18] and

---

* Author to whom any correspondence should be addressed.

hybrid material structures [19]. Research has also been carried out on the effects of ageing on hybrid polymers [20].

The wide range of proposed applications shows the need of a quality assurance tool case for fs-LDW. Test artifacts are 3D models with a certain set of features (e.g. geometrical, device-specific or technique-specific) that can be evaluated after the fabrication step. In other 3D Fabrication techniques like selective laser melting/sintering (SLM/SLS), test artifacts are already used to determine the quality of the test artifact itself and the current state of the machine such as the general additive manufacturing test artifact introduced by Moylan [21] in 2014. A highly-integrated test artifact that considers mechanical, geometrical and chemical analyzing methods was shown by Taylor [22]. Similar artifacts have also been shown for polymer additive manufacturing [23]. Due to the different materials and technology used for the mentioned test artifacts, portability of these existing artifacts to fs-LDW is not feasible, whereas the general usefulness of a test artifact for fs-LDW will be examined in this study.

To fabricate complex three-dimensional structures based on a given 3D model the use of a slicing software is needed. Generally, slicers split a model perpendicular to the fabrication direction into layers or 'slices' with a certain slicing distance d_z. To rapidly polymerize the solid parts of a slice, defined by its outer and inner contours by straight or curved lines, a 'hatching' process is used. The distance between each parallel line in a slice is called the hatching distance d_h. An optimization strategy must be determined: if the hatch distance is too large, the volume within the voxel may not be fully polymerized, but the fabrication time will be reduced. If the spacing is small, resulting in partial overlapping of exposure positions, this improves curing and costs time but can also lead to degradation effects [7, 24] and increases fabrication time. The cause of the dilemma is ultimately that the smallest volumes (voxels) are not cubes or cuboids that fit together perfectly in three dimensions and that are cured homogeneously. Nevertheless, this approach is and must be the basis of the digitally controlled guidance of the laser focus. Different studies on slicing approaches regarding the fs-LDW technique have been conducted [25–27]. Bauer *et al* [28] investigated the relationship between laser velocity, laser power and hatch/slice distance and found a mechanical enhancing effect at higher overlaps. On the other hand, an increase in size was also observed for SZ080, which also depended on the manufacturing direction [29].

A first set of proposed features for a fs-LDW test artifact was proposed by Baldacchini, LaFratta and Malinauskas [30, p. 222]. Lateral resolution was proposed to be measured by lines with variable lateral spacing. Lines that fall over were intended to measure the axial voxel height. A simple slab and T-shaped structure were intended to measure surface roughness directly or after the T-shape fell over. To measure shrinkage, a lollipop shape was proposed. The authors also outlined that the .stl file containing the test artifact has to have features smaller than the 'critical dimension of the writing system such that they are made in a single pass' to measure the voxel size itself. However the proposed features were not experimentally shown. Furthermore the measurability and repeatability

of structures that have to fall over or twist in a designed way has to be investigated.

In this paper, we first present the test artifact we devised and explain the rationale for its design in terms of the fs-LDW technique.

The goal of the test artifact is not to create perfect structures, but to create reproducible defects that can then be characterized for process optimization. The artifact is designed to be easily examined by the means of scanning electron microscopy (SEM) and light microscopy. Therefore those techniques are used primarily.

We then qualify and quantify the test artifact, which was initially made from an SZ2080 photoresist. Defects and analysis methods are shown from a variety of fabricated structures.

On a certain subset of the test artifact an investigation of the curing of OrmoComp photoresist is done via Raman confocal spectroscopy as SZ2080 with bis-photoinitatior had a high background by parasitic luminescence.

We perform a comparison between two different slicer software variants and explain the impact on geometrical aspects as well as on the general shape of the test artifact. In the last section, we use the geometric information as general design guidelines for optimized structures with more accurate geometric dimensions. In the supplementary information, structures fabricated on different substrates as well as a technical drawing of the test artifact and a .stl file of the test artifact can be found.

2. Experimental

2.1. MPLS platform

Fabrication of the test artifact was performed using a LaserNanofactory by Femtika, Lithuania, which incorporates a laser light source C-Fiber 780 High Power (Menlo Systems GmbH) operating at 100 fs pulse duration, 100 MHz repetition rate and 780 nm wavelength. The used immersion oil objective was a Zeiss Plan-Apochromat with a 63 × magnification and a numerical aperture of 1.4. The machine control software used was 3DPoli v6.33 by Femtika.

The used photoresists in this work are SZ2080 obtained from FORTH (Heraklion/Greece) and OrmoComp, obtained from MicroResist GmbH (Berlin/Germany).

2.2. Light microscopy electron microscopy

2.2.1. Micro Raman microscopy.
Confocal Raman measurements were performed with a confocal Alpha300R instrument (WITec, Germany), equipped with a 20 × Zeiss EX Epiplan DIC objective, a 532 nm laser (Excelsior 532-60) with a laser power of up to 20 mW. The spectrometer was an UHTS-300-VIS with two different gratings (see below) and a thermoelectrically cooled CCD-camera Andor DV-401A-BV-532 at $-64\,^\circ$ C.

For overview scans, a blazed grating called T1 with 600 grooves mm^{-1} was used, which is optimized for 500 nm and allows a scan up to a wavenumber of about 3800 cm^{-1}. In this case, a spectral resolution of three wavenumbers is

achieved in combination with a CCD camera with 1024 pixels. The laser intensity at 532 nm, which corresponds to a relative wavenumber of zero, is attenuated by several decades by an edge filter, but is usually still visible. Peak positions and peak widths are evaluated and serve to assess the quality of the spectrum over time. For a higher spectral resolution with an identical camera, the grating called T3 with 1800 grooves mm^{-1} (500 nm) offers a resolution of about one wavenumber, reducing the width of the possible scan to about one third. The instrument works in reflection mode. A glass fiber with a core diameter of 100 µm serves as the aperture of the spectrometer in the confocal setup. To reduce the local load on the sample surface, as large an area as possible of the designated square of the test artifact is scanned so that no local spot is burnt in. Wider scan fields include the substrate at the edge. Since the spectra of the test square show spectral bands of the glass substrate, these glass spectra can be used for the weighted subtraction.

3. A new test artifact for MPLS

3.1. Features (regions and properties)

The test artifact described here was optimized for a fs-LDW configuration that uses an immersion oil objective with an NA of 1.4 and a photoresist with a voxel size below 2 µm though it is easily adapted to other configurations through uniform scaling. Groups of individual components of the test artifact that, together, serve a calibration or test function are called 'features'. The design of the test artifact follows the general construction guidelines on test artifacts for additive manufacturing, which were published by NIST in 2012.

The requirements for these were laid out by Moylan *et al* [31], as:

- be large enough to test the performance of the machine near the extremes of the platform as well as near the center,
- have a substantial number of small, medium, and large features,
- have both holes and bosses to aid in verifying beam width compensation,
- not take too long to build,
- not consume a large quantity of material,
- be easy to measure, and
- have many features of a real part (i.e. thin walls, flat surfaces, holes, etc).

It was also pointed out by Byun and Lee [32] that 1) the minimum feature size should be determined, and 2) the features should be distributed on several axes in order to observe dependencies on the manufacturing location or direction. Since the scale of fs-LDW structures is much smaller than the test artifacts previously described for SLM/SLS, additional guidelines should be developed for fs-LDW test artifacts. Post-processing of the fs-LDW test artifact produced according to the procedures defined in this paper should ideally be limited to the addition of a conductive coating if necessary for SEM.

Table 1. Additional Constraints on fs-LDW test artifact design.

Constraint	Reason
Lateral size	Has to be larger than field of view
Height	Limitation of fabrication time
Distances between features	Minimal distance of 5 µm between each feature
Bulk/Non-Bulk	Surface attachment of bulk and non-bulk parts can be compared
Immersion indicator	Degree of immersion can be estimated
Feature sizes	Based on Reynards series following ISO 3 [38], similar for key features

This can be avoided altogether if the artifact is solely examined with optical microscopy (OM).

A variety of constraints have to be taken into consideration at the design of the test artifact. In the following we want to outline them. The minimum feature size, but also the shape of the voxel, and thus the resolution of the fs-LDW method is greater in the lateral direction than axial to the writing laser beam [33]. With lower NA the axial resolution of fs-LDW structures decreases more than in the lateral direction. The determination of the resolution perpendicular to the substrate can be problematic because in SEM and OM the sample must be tilted, leading to distortions. When viewing from the side, large substrates can be a hindrance to imaging; yet cutting them off risks jeopardizing the fabricated structure. With fs-LDW, features can be present that are of such small dimensions that they fall below the detectability of the OM [34], here confocal OM or scanning probe microscopy (AFM) may offer themselves as a possible solution. In the production of the test artifacts, the field of view (FOV) of the lens used for exposure plays a role, a feature that is also coupled to the magnification of the lens. To produce objects that are larger than the area accessible in the FOV, one must either work sequentially with partially overlapping fabrication areas (stitching) or use a so-called infinite field of view (IFOV) principle (see [35]). The IFOV principle combines the galvanic scanners with a servo stage for the purpose of a combined scanning movement. The boundary conditions derived therefrom for the construction of the artifact were determined as shown in table 1.

The shown test artifact can be used for a variety of purposes in the 2PP process. Those include the influence of different baking temperatures or times, different developer solutions as well as the drying in a critical point dryer on the resulting geometrical as chemical properties of the test artifact. The test artifact can be an aid to get geometric offset information, which is needed for high-accuracy applications as shown in [36, 37]. To evaluate new photoresists the fabrication of arrays of structures with individual laser power and speed is an established and fast procedure to access the processing window. The test artifact can then be an aid to compare between parameters inside of a predetermined process window.

The individual features of the test artifact are shown in figure 1 and further explained in table 2.

The outer ring feature (#1) is a ring with a diameter of 400 µm and a height/width of 5 µm. The ring thus expands
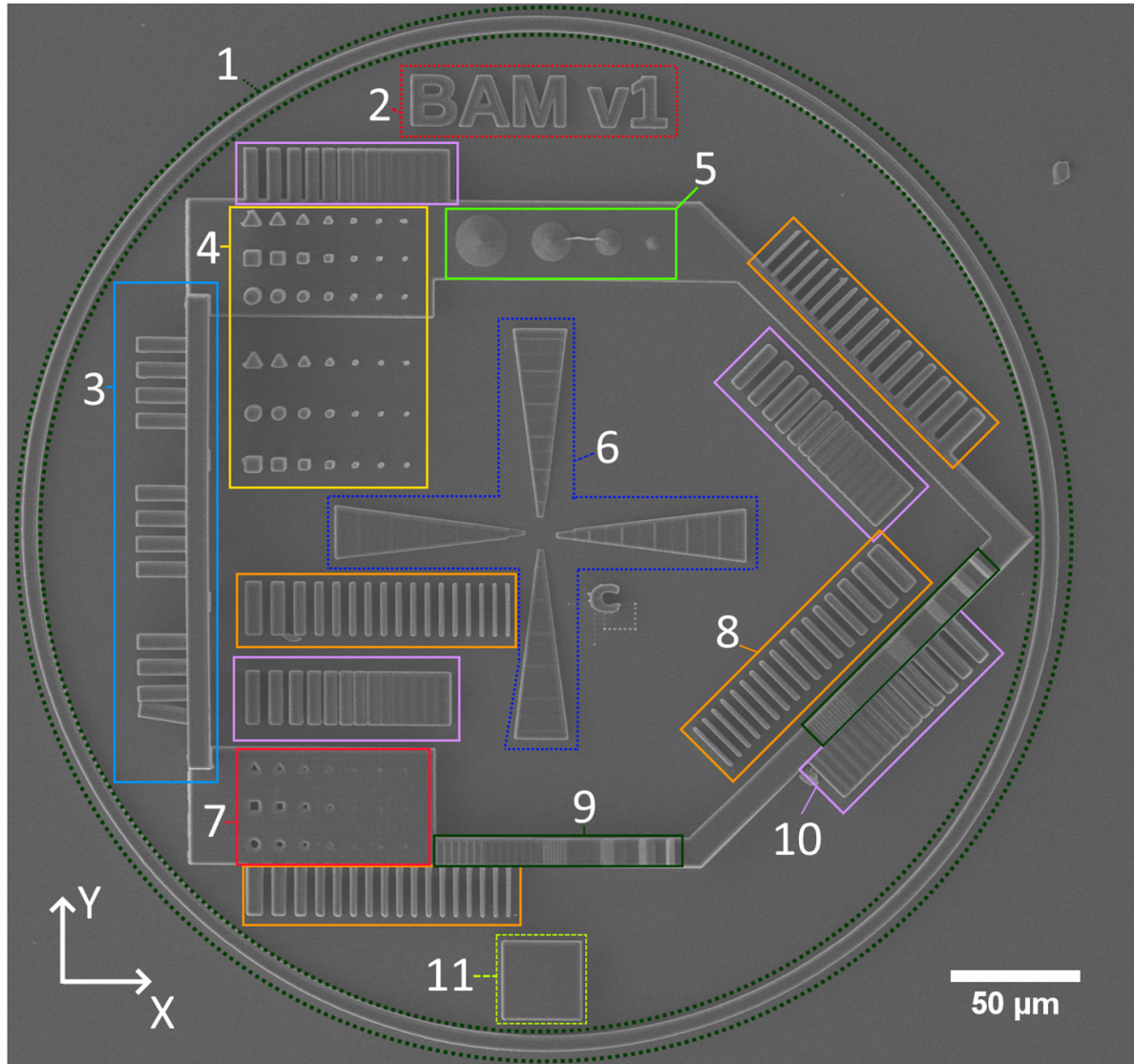
Figure 1. Overview SEM image of a test artifact with highlighted features as shown in table 2, fabricated with SZ2080, 12 mW laser power and a velocity of 7000 μm s^{-1}, d_h 0.2 μm, d_z 0.2 μm, indicated features are described in table 2.

outside of the FOV of the lens, thus testing the interaction of multiple stages or stitching method used for writing larger structures. In addition, information about the tilt of the substrate can be obtained, as tilting changes the height of the ring locally; with heavily tilted substrates, part of the ring may even disappear or be delaminated, since the laser focal point is completely incorporated into the substrate.

The version indicator (#2) is used to differentiate between the current and upcoming versions of the test artifact.

The 'Z spacing' feature (figure 2) (#3) consists of 12 identical bars, which are placed freely in space without binding to the gate above. The free distance between the bars and the gate starts at 1 μm (figure 2, light grey left side) and increases in 0.5 μm steps to a maximum of 5.5 μm (dark grey, far right). Since the cross-linked voxel can be approximated as a rotational ellipsoid with high expansion in the *Z*-direction, an unintentional solid connection occurs at a distance of 1 μm from the portal. The reason is that both the height of the free

bar and the height of the portal are larger than defined in the fabrication script due to the added voxel height. As the distance increases, the connection between the bar and the gate is reduced to a thin thread, which leads to a dislocation of the bar or even to a detachment from the gate when the stabilizing monomer gel is washed away during the development process. This makes it possible to estimate the vertical fabrication precision, and the overlap of the successive layers, respectively.

The Rods feature (#4) consists of triplets of shaped rods with a height of 20 μm of decreasing lateral dimension. Each triplet consists of a square, triangular and round rod, with similar lateral chord lengths. The rods are placed once directly onto the substrate and once on a base body to observe the influence of substrate adhesion. With the reduced chord lengths, the accuracy of reproducing geometric shapes at smaller diameters can be estimated. The corresponding feature #7 has the same shape as the rods in the bulk body and can be used to

Table 2. Naming of individual features of the artifact as shown in figure 1.

Number	Feature	Explanation/reasoning
1	Outer ring	Determine substrate tilt
2	Version indicator	
3	Z spacing	Free space in Z direction
4	Rods	Geometrical accuracy
5	Cones	Shutter artifacts
6	Immersion indicator	Fabrication depth in substrate
7	Holes	Geometrical accuracy
8	Thin walls	Geometrical accuracy
9	Staircase control	Influence of slicing height, staircase effect
10	Gaps	Geometrical accuracy
11	Test pad	Chemical and physical measurements
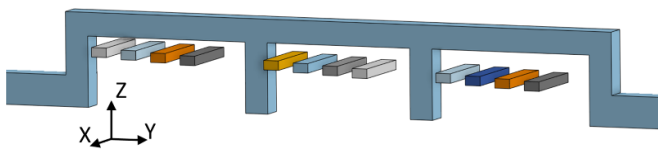
Figure 2. Tilted CAD view of the 'Z spacing' feature (#3) with the top portal and two pillars (blue), the 12 unattached bars, with increasing space from left to right, are placed underneath and shown in different colors.

estimate the replicability of fabricating negative shapes in the *XY* plane.

The cone feature (#5) placed on the bulk body consists of four spherical cones with an angle of 45° and a diameter of 5–20 µm in 5 µm steps. Due to the slicing process each cone will be separated in circles with a decreasing diameter. The feature can be used to observe the shutter properties as for each circle the shutter has to be opened and closed at precise locations. Deformations along these cones are possible due to problems with the shutter timing or the chosen slicing profile.

To find out how well the test object is connected to the substrate in comparison with the preset fabrication depth, the immersion indicator (#6) is positioned in the center of the artifact. This consists of four wedges whose height decreases towards the center. With a length of 80 µm and a maximum height of 5 µm, a very low incline (≈3.6°) is obtained and the object is thus very sensitive to the starting depth of writing on the substrate. Therefore, if e.g. only half of the immersion indicator is visible the whole test artifact has been fabricated about 2.5 µm into the substrate. To ensure intercomparability between test artifacts we propose that the maximal immersion is less than 2.5 µm, which corresponds to a distance between the remaining immersion indicator wedges of 80 µm. It must be noted that the wedges are not angled towards the substrate due to the staircase effect and therefore the distance between the individual steps depends on the slicing height. Using e.g. an AFM or confocal OM, a determination of the thickness of a sliced plane is easily determined. Figure 3 shows the effect and resulting shape.

The thin walls (#8) and gaps features (#10) are used to assess the geometrical accuracy of the system. Both features are either freestanding or attached to the bulk body to examine the influence of the substrate and for the attached features the influence of the slicing method. Both features are additionally fabricated at a 45° angle to observe the diagonal feature precision.

The staircase feature (#9) consists of five pyramids with a height of 5 µm on top of the bulk body. Their angle is gradually increased by 15° from 15° to a maximum of 75°. The feature is repeated in a 45° angle on the bulk body for the influence non-perpendicular features have on the staircase effect.

The test pad feature (#11) is a simple cubic structure with a side length of 30 µm and a height of 10 µm. It can be used for methods such as confocal Raman spectroscopy, microindentation or white light interferometry to analyze chemical, mechanical or structural properties.

Furthermore, transmission can be measured at the test pad feature with a microspot light source as needed for the fabrication of optical structures, see [39].

3.2. Test pad evaluation via confocal Raman spectroscopy

The effect of light intensity during the writing process and possible post-curing by daylight changes the cross-linking density of the fabricated structure. This can affect the dimensional stability of the structure and its optical and mechanical properties. Therefore, the test pad feature is evaluated via micro Raman microscopical comparing of two test pads fabricated with 12 and 18 mW of writing laser power, respectively. First, the chemical composition, the curing reaction and the assignment of the Raman peaks to the different chemical groups is discussed. Then it is shown that it is possible to follow the progress of the photoreaction under exposure to the fs laser at 780 nm.

Raman experiments with SZ2080 photoresist failed due to the dominance of fluorescence over the Raman intensities (see Suzuki *et al* [40]), so here only the Ormocomp™ photoresist is used and evaluated as a model system. A description of the Ormocomp™ precursor or network is unfortunately not clearly described in literature, only the dissertation by Obi [41] contains corresponding information in the form of a structural formula. The formula given there shows a chain based on –O–Si–O–Si units to which polymerizable side groups are attached. This side group starts with a propanethiol as a spacer to the silicate chain and branches into a three-armed structure. This in turn consists of a quaternary carbon atom with three attached structural elements of acrylic acid and an ethyl group. Two still reactive vinyl groups of the acrylic acid remain in the structural unit, the third served for the connection to the spacer (see figure 4). It is not certain that the description of the precursor is complete, but further information could not be obtained. To the best of our knowledge, no information is known about any photoactivators or other additives in the Ormocomp formulation used. The incomplete information nevertheless provides an important guidance with regard to the interpretation of the Raman spectra.
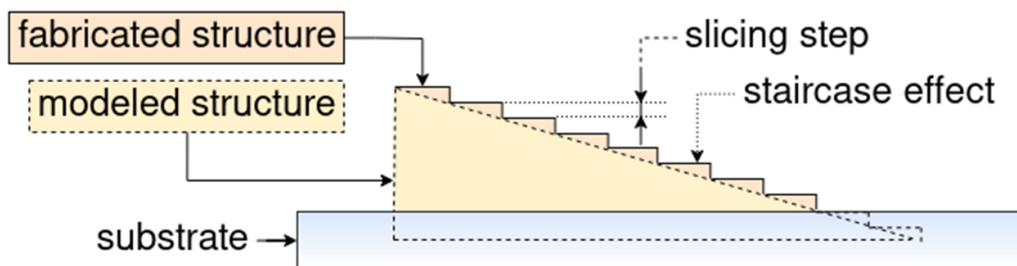
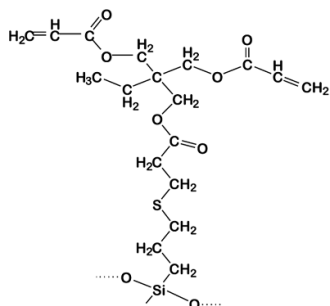**Figure 3.** Schematic illustration of staircase effect and resulting structure.

Figure 4. Chemical composition of the precursor of Ormocomp, after Obi [41].

Figure 5 shows Raman overview spectra of the photocurable resin after exposure with different powers, 12 and 18 mW. After taking into account the Raman response of the glass substrate and a background correction, the spectra are almost congruent with each other. A calculation of two weighted differences of the spectra shows the deviations more clearly (figures 5(d) and (e)).

Only a few literature references could be found for the assignment of Raman peaks to chemical groups. Raman spectra of Ormocomp describing the 2PP process in the range 1400–1800 cm^{-1} can be found in Rys *et al* [42] with a spectral resolution estimated at 1 cm^{-1}. Spectra from literature often show spectral ranges for the groups and only rarely sharp peaks. This is due to the chemical environment of the groups. The range around 1630 cm^{-1} is assigned to the reactive (H2C=CH–) double bond, a group whose concentration and thus signal strength decreases with progressive photopolymerization. In the spectra, additionally, a strong peak at ≈1740 cm^{-1} appears [43], which is related to the carbonyl bond (O=C–), as also found in [42]. The difference spectra show two main areas of deviation in form of positive peaks at ≈1630 and ≈2900–3100 cm^{-1}. Positive peaks mean that the concentration of the associated group was even greater at 12 mW exposure strength than after 18 mW power input. Conversely, this means that photo-curing with the fs pulse laser consumes these groups. In figure 5(e), a negative peak for carbonyl (≈1740 cm^{-1}) is found additionally. Let us not forget that the recording of the two spectra required a change of sample, whereupon a new positioning of the focal distance must be made in confocal microscopy spectroscopy. For this reason, the slight differences in the spectra caused by this must be compensated for by a method that requires knowledge of the

molecular groups, their band position and the most probable chemical reaction that has just been worked out. If the difference of the spectral intensity $I(v)_{12mW} - f \cdot I(v)_{18mW}$ is formed and the intensities for the peak at 1740 cm^{-1} (carbonyl) are minimized, $f = 0.83$ applies. If the sum of all intensities is compensated to zero, the correction factor $f = 0.9285$ leaves a negative peak in the carbonyl range.

Let us first inspect figure 5(d) more closely. If we look at the peaks in the spectra in figure 5(c), we see that the result of the difference formation in the range between 600–1500 cm^{-1} is not very clear. The differences are always small and exhibit considerable noise, which reduces their significance. Only a few peaks can be unambiguously assigned, e.g. the positions marked with a yellow rhombus could belong to thioether linkages of various kinds [44], but their assignment is not certain. We therefore refrain from an interpretation of these peaks. Assuming that the chemical composition of OrmoComp given in figure 4 is correct and in particular complete, only the vinyl groups (H2C=CH–) should be involved in the photoreaction with the fs-laser light. An analogue is the reaction of acrylic acid to polyacrylic acid, which proceeds via a radical mechanism. In this case, the concentration of the carbonyl groups (O=C–) does not change and a weighting factor of 0.83 fulfils this condition for the peak at ≈1740 cm^{-1} as well as possible. Consequently, the difference peak at 1630 cm^{-1} is positive because the concentration of the vinyl group decreases with stronger exposure. The only other meaningful area is the range between 2800 and 3100 cm^{-1}. It contains the most diverse chemical groups and is difficult to evaluate with a structure that is not completely known. Nevertheless, it should be recognizable that the vinyl group (3058–3080 cm^{-1}) is consumed, this is true, the peak is positive. During the reaction, different species are consumed and according to the reaction scheme new species are formed. For example, one methine group ormethanetriyl group (>CH–) and one methylene bridge (methanediyl group, –CH2–) are formed per reacted vinyl group (H2C=CH–) at the acrylic end. There, the difference should be negative, which is obviously not the case in figure 5(d). According to the state of knowledge about the compound, this cannot be the case, which makes the first choice of the weighting factor implausible. However, this also means that the idea of the inert nature of the carbonyl group in the photoreaction must be abandoned. Figure 5(e), on the other hand, shows a difference spectrum with a weighting factor of 0.9285 that gives the value zero as the sum of all intensities. It is 12% higher than the value in figure 5(d). In
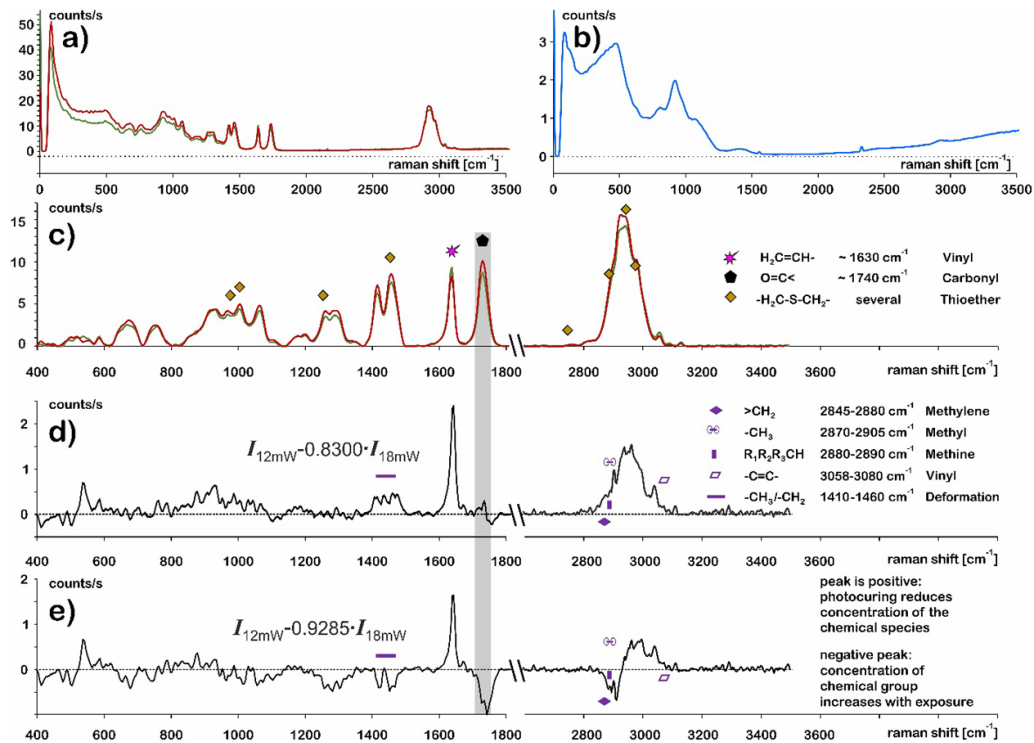
Figure 5. Raman spectra of Ormocomp™ (a) and (c) and the glass substrate (b) as well as two difference spectra (d) and (e) of a photo-curing in the fs-LDW machine at 1080 nm, measured with grating T1 (3 cm^{-1}). (a) Raw data spectrum after the fabrication process with 12 mW line power of the laser (green line) and with 18 mW (red line). A comparison with the spectrum of the glass substrate in (b) shows the necessity of a weighted subtraction, the result is shown in (c). The difference spectrum (d) and (e) positively weights the data at 12 mW and subtracts from it the curve belonging to 18 mW. The weighting factor of ≈ 0.83 in (d) was chosen under the assumption that the concentration of carbonyl bonds remains constant during light curing and ageing and that therefore the difference of the two spectra at the grey marked position should be as close to zero as possible. The weighting factor of 0.9285 in (e) was chosen so that the sum of all intensities is zero.

this case, the range between 2800 and 3100 cm^{-1} splits into a positive (species are consumed) and a negative (species are produced) range. It is understandable that methylene groups (2845–2880 cm^{-1}) and methine groups (2880–2890 cm^{-1}) [43] are generated when the vinyl group reacts. The generation of methyl groups (2870–2890 cm^{-1}) neither fits to the chain generation nor to the termination reactions of a radical polymerization of acrylic acid. In contrast, however, the deformation oscillation of the methylene group (1410–1460 cm^{-1}) also appears as a negative peak, which correctly corresponds to the result of the polymerization. The range between 2930 and 3080 cm^{-1} reflects the consumed species, the vinyl group lies in this range, but the assignment of the remaining Raman bands is unknown. It is clearly visible, however, that a negative peak is formed at 1740 cm^{-1}, i.e. carbonyl groups should be formed. Reaction pathways could be found for this, but not proven within the scope of this work. For example, one would have to assume the participation of atmospheric oxygen in the photocuring process. A possible reaction with oxygen can be well justified: The existing pre-polymerization via the silicate chain, which is present in the precursor, leads to a steric hindrance at the reactive vinyl group.

If these are activated radically, they need sufficient proximity to the next vinyl group. If this cannot be achieved, the activated chain ends can only be saturated with oxygen, which

explains the generation of carbonyl groups with increasing exposure.

In the future, photopolymerization with the exclusion of oxygen is being considered, but this would involve some effort.

It remains to be noted that the degree of curing by the fs laser can be determined by means of Raman microspectroscopy on an appropriately constructed test artifact.

In this case it would be advantageous to avoid signal components of the substrate, because finding the correct weighting factor is not error-free. One solution would be to increase the thickness of the object at the landing site intended for Raman measurement. A lens with a higher magnification and a shorter focus length could also be used.

3.2.1. Post-curing reaction induced by laser beam exposure: synthesis and degradation. The cured sample (fs-laser 780 nm at 18 mW, see difference spectrum in figure 5) was further investigated with the aim of determining its stability. Further formation of the networks during visible light exposure can alter dimensional stability, adhesion to the substrate and mechanical properties. The laser of the Raman microscope (532 nm) serves as a light source and exposes a spot with a diameter of 3–4 µm. The use of polarized light opens up greater sensitivity to change as the orientation of the groups
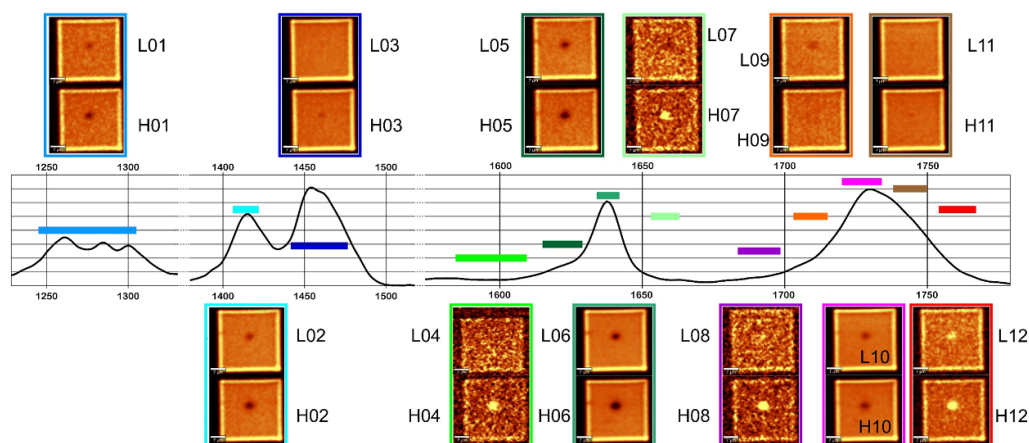
Figure 6. The result of hyperspectral imaging of the artifact at the position dedicated for Raman spectroscopy, measured with grating T3 (1 cm^{-1}). Incoming laser beam at 0° (polarizer position), analyzer at 0° (∥). The laser load is described by the two letters L and H (L = low, H = high), L means a period of a max. 4 h, which is required for focusing, distance optimizing to maximum Raman yield and measurement of spectra. H corresponds to an additional exposure time of 14 h at the identical position of the sample. The Raman spectrum in arbitrary units is an average spectrum of an unpolarized measurement of the hole area as a guide to the eye. The color-coded sections in the spectrum were selected according to the distinctness of the exposure results. The abscissa was interrupted twice for the purpose of clarity of the representation at sections without spectral information.

changes. Exposure for an additional 14 h was used to investigate whether subsequent changes occur at this already pre-cured position. Since the wavelength of 532 nm (2.33 eV) used for Raman measurements is about as high as the energy of two photons of the pulse laser (1080/2 = 540 nm corresponding to 2.3 eV), such changes are not unexpected.

The experiment is performed with polarized light (532 nm), at first with analyzer parallel to the incoming beam (∥), at second with crossed polarizers (⊥). The light used by the laser is originally already linearly polarized, but the beam guide contains an optical fiber on the illumination side that partially depolarizes the light. Therefore, a polarizer is set to maximum intensity at the strongest Raman peak. This setting of the polarizer is set to correspond to zero degree (∥, 0°). The measurements of the Raman light are then analyzed with the analyzer parallel (∥, 0°) and perpendicular (⊥, 90°) to this position in order to gain initial insights into any anisotropy of the sample and corresponding changes during a possible photo-chemical reaction. When exposed to linearly polarized light, it turned out that mostly an attenuation of the response intensity is found in the middle of the square, e.g. at wavenumbers 1441–1476 cm^{-1} (marked in cyan) as to be seen in figure 6. It can be concluded that at this position, which is used to adjust the focus, an increased amount of light causes bleaching by destroying the underlying molecular bonds. While the exposed center is usually subject to a slight to severe loss of intensity after ≈4 h (labeled L) and ≈18 h (labeled H), there are also spectral regions in which this is reversed. This applies to the rising or falling flanks of the region of the vinyl bond by 1630 cm^{-1} and the carbonyl region by 1740 cm^{-1}. Since it has already been shown that with increasing exposure to light at 532 nm, the vinyl concentration decreases overall, this slight increase suggests a chemical change in the environment of the still existing vinyl bonds. Accordingly, the local concentrations of the various carbonyl bonds also change. The

very probable involvement of dissolved atmospheric oxygen has already been pointed out.

The experiment is performed with polarized light (532 nm), first with the analyzer parallel to the incoming beam (∥), and secondly with crossed polarizers (⊥). The light used by the laser is originally already linearly polarized, but the beam guide contains an optical fiber on the illumination side that partially depolarizes the light. Therefore, a polarizer is set to maximum intensity of the Raman spectrum.

When exposed to linearly polarized light, it turned out that mostly an attenuation of the response intensity is found in the middle of the square, e.g. at wavenumbers 1441–1476 cm^{-1} (marked in cyan) as to be seen in figure 6. It can be concluded that at this position, which is used to adjust the focus, an increased amount of light causes bleaching by destroying the underlying molecular bonds. While the exposed center is usually subject to a slight to severe loss of intensity after ≈4 h (labeled L) and ≈18 h (labeled H), there are also spectral regions in which this is reversed. This applies to the rising or falling flanks of the region of the vinyl bond by 1630 cm^{-1} and the carbonyl region by 1740 cm^{-1}. Since it has already been shown that with increasing exposure to light at 532 nm, the vinyl concentration decreases overall, this slight increase suggests a chemical change in the environment of the still existing vinyl bonds. Accordingly, the local concentrations of the various carbonyl bonds also change. The very probable involvement of dissolved atmospheric oxygen has already been pointed out.

Comparing these results with measurements with crossed polarizers (Pol 0°, Ana 90°) gives the same picture. As expected, the Raman intensity is smaller with crossed polarizers, so only the signal to noise ratio is smaller. Further differences are not detectable, which is why an evaluation of the local degree of polarization, e.g. is not carried out. In summary, at least under the parameters chosen so far for the fabrication of the
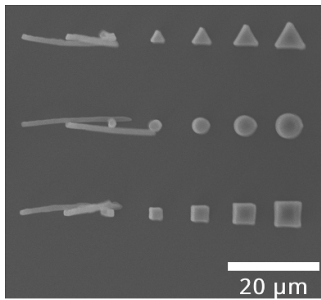
Figure 7. SEM image of rod feature (#4) directly on the substrate, partially collapsed are the smallest three rods of each geometry, SZ2080, 6 mW, d_h 0.2 µm, d_z 0.4 µm, 3DPoli sliced.
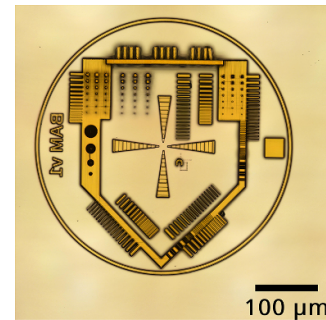

Figure 9. Light microscopy image of a test artifact SZ2080, 8 mW, d_h 0.2 µm, d_z 0.4 µm.
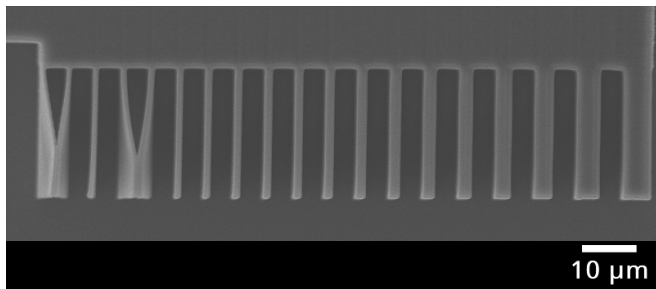

Figure 8. SEM image of thin walls (#8) attached to bulk, partially collapsed, SZ2080, 6 mW, d_h 0.2 µm, d_z 0.2 µm, 3DPoli sliced. Scale bar 10 µm.
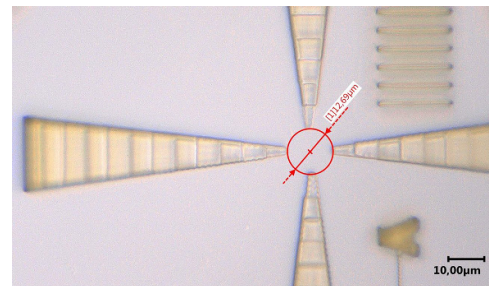

Figure 10. Digital microscopy image of the immersion indicator with a distance between the start of the immersion indicators of 12.69 µm and a calculated intrusion depth of 0.39 µm. SZ2080, 12 mW, d_h 0.2 µm, d_z 0.4 µm.

test artifact, no reorientation of bonds occurred during ageing in visible light. We assume that the last vinyl groups were able to react, and these are already so anchored in the network that only little rotation, i.e. reorientation, is needed.

3.3. Qualification

In the following a selection of typical error patterns and informations from different test artifact structures is presented with the aim of representing the features. With the described geometrical features an insight in the relationship between photoresist and its adhesion on the substrate can be gained. If the adhesion between the structure and the substrate is too low, the individual bar will collapse or fall over. This can be seen in figure 7. All rods smaller than a predefined size of 2 µm collapsed with the used parameter set of the fabrication process. Similar behavior in the collapse of the thin walls attached to the main structure can be seen in figure 8, where the mechanical strength appears to be too low. The thin walls are deformed by mutual attraction but are still attached to the substrate.

A partial analysis of the test artifact can be done by light microscopy. We evaluated multiple test artifacts with light microscopy, confocal laser scanning microscopy and a digital light microscope. Collapsed features as previously shown can also be examined with these methods (not shown). An overview image of a test artifact is given in figure 9. As already described above, size and symmetry of the immersion indicator helps to assess the Z-position of the first slicing plane and to predict the achievable adhesion to the substrate. An

immersion indicator evaluated by light microscopy is shown in figure 10. In this case it can be estimated that the first Z-layer is about 0.39 µm below the glass plane.

The test artifact was further fabricated with OrmoComp photoresist, which is shown in the supplementary information. The test artifact can also be fabricated on different substrates like silicon wafers, polyethylene terephthalate foil or steel discs. The different substrate properties like roughness, reflectivity or adhesion with photoresists influence the test artifacts quality.

3.4. Adapting for different optics

The data presented is based on the use of an oil immersion lens with a numerical aperture of 1.4, but working with air/dry objectives is also possible. Dry objectives have a smaller numerical aperture and therefore the voxel size is stretched along the *XY* axis and by a larger factor in the *Z* axis, as shown by [45]. The test artifact should therefore be scaled independently for *XY* and *Z* axis. The hatching and slicing distances have also to be adjusted to ensure a reasonable voxel overlap and fabrication times. The energy distribution in the focal area of the objective estimated via the Gaussian beam can be a guideline to estimate those values. To fabricate the test artifact with an 0.95 NA objective we used scaling by a factor of 1.5 in *XY* and 2 in *Z*, resulting in a diameter of 612 µm and a height of 60 µm. Hatching d_h and slicing d_z distances were set at 0.4 and 0.6 µm, respectively. The resulting structure can be seen in figure 11. The measured feature sizes are shown in table 3.
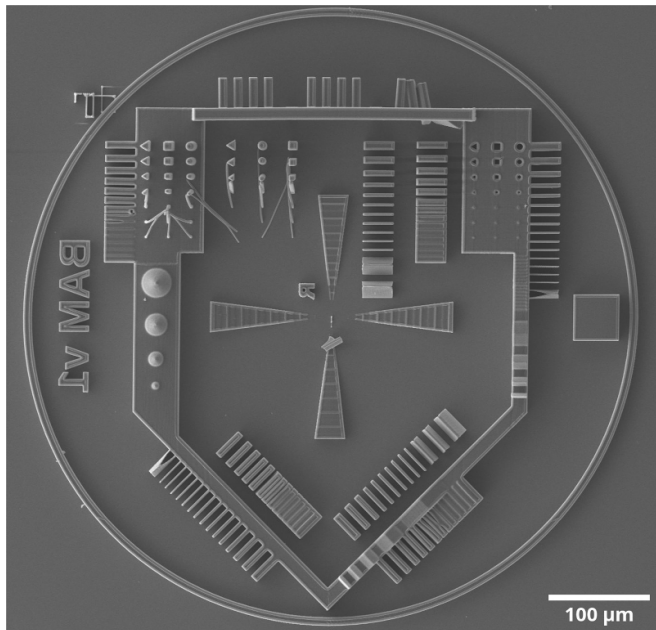
Figure 11. SEM image of a test artifact fabricated with a 0.95 NA dry objective, SZ2080, 12 mW, 7000 μm s^{-1}, 612 μm diameter, 60 μm height, d_h 0.6 μm, d_z 0.8 μm, 3DPoli sliced.

It has to be noted that due to the different scaling in the spatial directions the angles, e.g. of the cone feature, are distorted.

3.5. Limitations

The test artifact may not be directly applicable to very flexible materials or combinations of photoresist and photoinitiator where photopolymerization is done with a voxel size large enough to make the evaluation of certain features as the Z-spacing or thin walls impossible. For those combinations the current spacing between the individual features must then be changed to obtain a benchmark.

Furthermore, individual features can currently not be extracted and individually fabricated. This would be beneficial for requirements, where only a certain set of features is needed. Such an approach would lower the fabrication time, while still working with a refined set of features from a known test artifact.

For fs-LDW setups without a combined stage movement the fabrication time may be significantly higher than the 15 min fabrication time achieved on the shown system. Those systems also have to rely on stitching to generate structures.

4. Practical applications

4.1. Influence of slicers on test artifact

As an application example for the presented test artifacts, we want to investigate the influence of two different slicers on the above mentioned properties of the test artifacts. Slicers are an integral part of fs-LDW production technology. Slicers developed with fs-LDW in mind have been proposed in the literature with a sub-regional slicing approach by Park *et al* [46]

and an adaptive slicing method using the tilted voxel by Zheng *et al* [47].

However both methods are currently not available either open-source or as part of the used fs-LDW setup itself. A review on the considerations for slicing approaches in fs-LDW can be found in the work of Zhou *et al* [2]. The shape and geometric accuracy as well as the mechanical or optical properties of the resulting structure partially depend on the tool path the slicing software generates from the given 3D model as well as the parsed parameters [48, 49]. For example, a cube with a side length of 4 μm cannot be cut with evenly distributed lines at a hatching distance of 0.3 μm. The lines must be distributed either more densely or more sparsely. This changes the overlap between the voxels and therefore the mechanical properties also change. For SZ2080, it has also been shown [29] that the time between each manufactured line or cut distorts the shape of a structure.

The 3DPoli software provided with the fs-LDW machine used in this study, has an integrated slicing component where hatching and slicing distance as well as the option for an outer contour line can be set. GCode from other slicers can be imported into 3DPoli via a command. For comparison, we used the 3DPoli slicer and Cura v6.11, an open-source slicer, which is mainly developed with fused-deposition modeling (FDM) printers in mind. The Cura slicer is not optimized for fs-LDW technology. The sizes given in the GCODE must be divided by 1000 to get from the sizes used in Cura (millimeters) to the micrometer units used by default in fs-LDW manufacturing.

The main dissimilarity between the slicers is the way an object's slice is filled with tool paths to be moved along. In figure 12 the difference between the two slicing approaches can be seen. In Cura, we use 4 outer shells and 100% fill to fully polymerize a slice, alternating hatch lines along the X/Y axis for each slice. For features oriented at a 45° angle to the XY axis, both slicers also use a different approach. The 3DPoli slicer uses short lines along the X/Y axis, while the Cura slicer moves the ray along the contour line of the feature and only switches to perpendicular hatch lines above a certain geometric threshold.

The chosen beam path by the slicer has an impact on the resulting geometrical accuracy. In figure 13 a partial enlargement because of a missing beam width offset is shown. The parameters for hatching, slicing, laser power and velocity have not been changed to enable comparability of both slicers. The additionally used parameter set can be seen in table 4.

The following parameter set was used for both slicers: a laser power of 8 and 12 mW respectively, beam velocity 7000 μm s^{-1}, a hatching distance d_h 0.2 μm and a slicing distance of d_z 0.4 μm. Resulting in a fabrication time of 15 min 42 s per test artifact.

To compare the test artifacts we will show a subset of features. Thin walls and the hole features were measured via SEM. As the subsequent information of the following measurements is similar, the rest of the features that were measured are shown in the supplementary information.

In figure 14 the measured sizes are compared between the two slicers and laser powers. Ideally, the measured sizes correspond to the nominal size, i.e. the size of the feature in the

Table 3. Observed features and results from the analyzed test artifact fabricated with a 0.95NA objective, only minimal feature sizes are given.

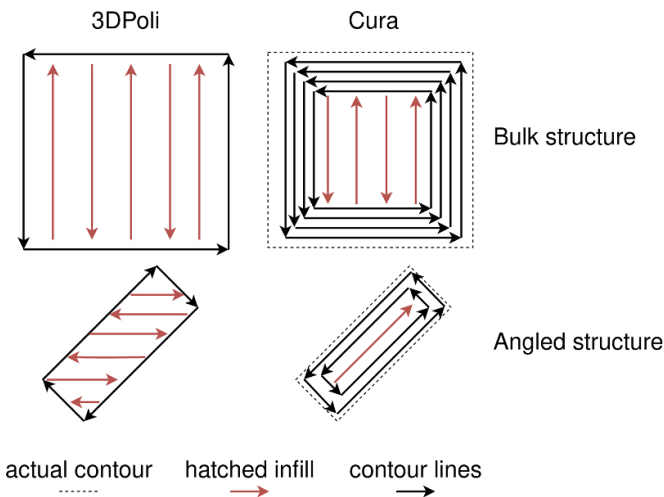| Feature	Results	Comment
Thin walls		
on substrate	6 walls collapsed, min. 1.9 μm	no difference between 0°
attached to bulk	2 walls collapsed, min. 1.7 μm	and 45°
Gaps		
on substrate	min. 2.1 μm	no difference between
attached to bulk	min. 1.4 μm	substrate or bulk at 45°
45°	min. 2.1 μm	
Rods		
on substrate	3 attached, min. 5.4 μm	
on bulk	4 attached, min. 3.5 μm	
Holes	4 open holes, min. diameter 2.2 μm	
Z spacing feature	Attached: 8 Distorted: 3 Gone: 1	min. Z distance: 6.5 μm

Figure 12. Simplified illustration for the chosen beam paths of 3DPoli and Cura slicer, red hatched infill and black arrows outer contour lines shown for a simple cubic geometry and a 45° angled thin wall.
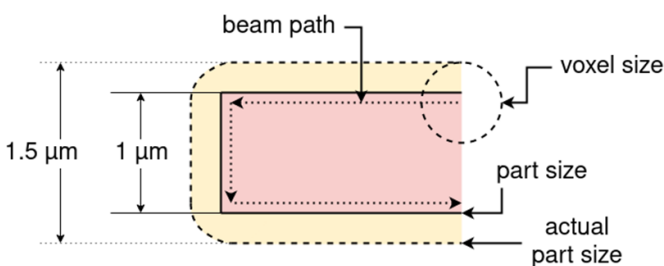

Figure 13. Schematic illustration of the connection between voxel size, beam path and the resulting shape.

Table 4. Settings in 3DPoli and Cura Slicer.

Slicer	3DPoli	Cura
Parameter	Contour shell before hatching	0.2 mm layer height
	Contour shell = True	0.2 mm nozzle size
		Wall line count = 4
		Infill line directions = [0, 90]
		Print thin walls = True

thin walls features sliced with 3DPoli, the measured sizes were higher than Cura sliced ones. The difference between the two slicers was lower for the higher laser power. Thin walls with 45° alignment showed a more similar behavior where the 3DPoli sliced walls were larger but with a smaller offset. The lower wall thicknesses for Cura sliced walls can be partially explained by the internal offset for the squished filament under the nozzle of a FDM printer. However, as the Nozzle Size in the parameters was set to 0.2 mm, the offset is only 0.1 mm in the original GCODE or 0.1 μm in the fs-LDW process. For the thin walls feature the Cura slicer showed a slightly different behavior, where the offset partially decreased with the increasing size of the thin walls. For larger dimensions, the real dimensions of the thin walls are thus closer to the values of the test artifact. The gap's features show a similar behavior to the features shown previously, the geometric accuracy is higher for the test artifacts sliced with Cura. At 8 mW Laser Power the Cura-sliced sizes are nearly identical to the nominal sizes but a higher scattering is noted, as shown. The longer line for Cura sliced artifacts in the gap feature represents those gaps that are not grown together compared to the 3DPoli-sliced ones at small gap distances.

The produced test artifacts can also be compared qualitatively. A comparison of the cone feature between both slicers can be seen in figures 15(a) and (c). The 3DPoli feature has a pronounced stair-step effect and a small dent on the left side, possibly due to similar starting points for each slice. On the cone cut in Cura, the staircase effect is less visible, but a prominent line was observed on the right side. The Cura slice here shows its origin from the FDM process, as we assume that this line comes from the seam line and a pronounced wiping

model. The so-called nominal sizes are given as green dashed lines. With both slicers the features are fabricated either too large (positive size difference) or, in the case of the gap feature, the distance between the adjacent walls is too narrow and the gap closes too early (negative size difference). If the line of the measured sizes runs parallel to the nominal sizes a general offset can be applied to get a correct size. For the
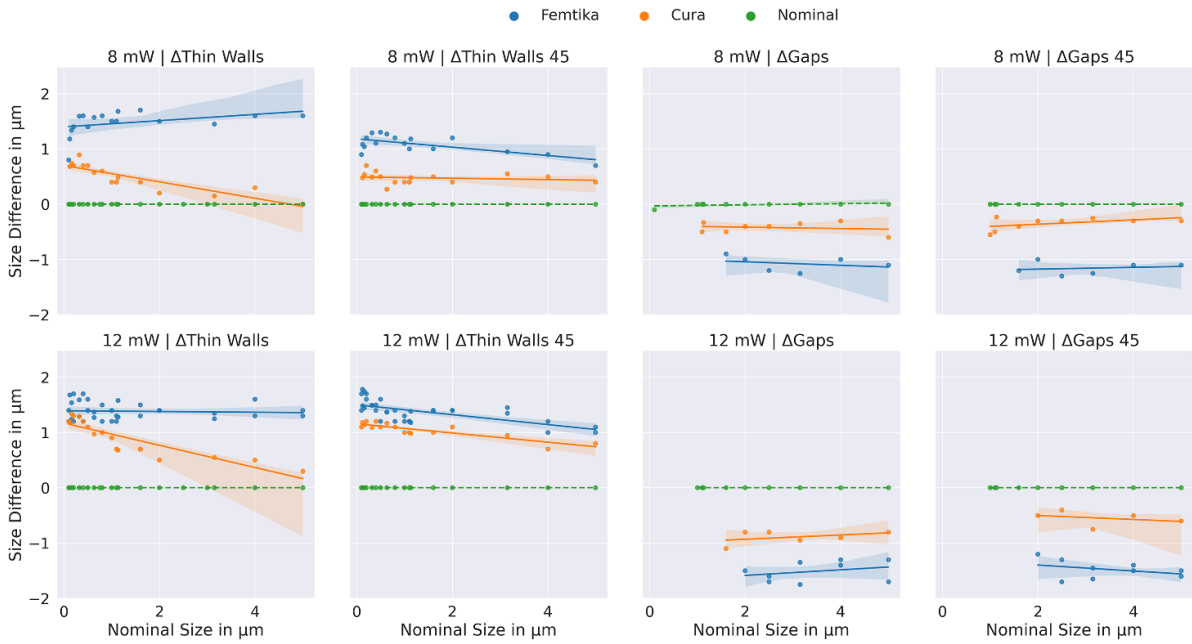
Figure 14. Deviation from nominal size (green dashed line) for thin walls and gaps features (both also in a 45° angle) at different laser powers per row and for different slicers, a 95% confidence interval is given for the fit line.
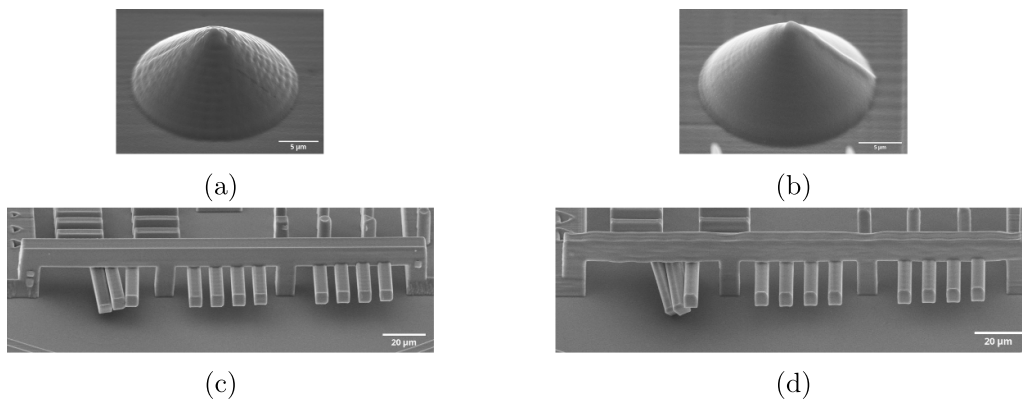

Figure 15. SEM images of cone and Z spacing features sliced with (a) and (c) 3DPoli or (b) and (d) Cura respectively.

process performed to remove unwanted molten filament from the nozzle. This defect can probably be eliminated by a further fine tuning of the Cura parameter set.

To compare the general quality of the difference between the 3DPoli-sliced figure 15(c), and the Cura-sliced figure 15(d), a tilted view on the Z-spacing feature was picked. On the 3DPoli sliced structure on the left pillar side shows a reproducible slight bending towards the middle, which we attribute to the shrinkage of the SZ2080 photoresist. The 3DPoli sliced structure shows a very high sharpness and with no visible deformations on the bulk surface. The bars on the right side are heavily merged with the support beam, whereas the more left ones are only slightly attached. It has to be noted that the top surface of the top bar seems to be dented above each of the pillars which could indicate incomplete curing of the photoresist even though the same laser power and

velocity, as well as hatching distance, was chosen. We assume a problem in the interpretation of the GCODE in the 3DPoli software. The structure sliced with Cura, on the other hand, had a wobbly surface with unsharp edges. Interestingly a similar amount of attached bars can be found on both structures as the intrusion of beam and bar is similar. This is an indication that laser power, hatching and slicing distances play a more important role than the slicer used.

Design parameters can be calculated from the collected geometric measurements by subtracting the offset obtained from the measurement of each feature. These design parameters apply to the same set of parameters with which the test specimen was manufactured. The required offsets in the *Z*-direction can only be estimated with this test artifact, as no special function for construction parameters parallel to the substrate has been implemented.

5. Conclusion and outlook

With its unique manufacturing technology and the outstanding resolution fs-LDW offers a wide range of applications. To build a resilient quality, infrastructure is therefore needed to broaden the acceptance of fs-LDW as a reliable fabrication technique. The shown test artifact was shown to work on different substrates as well as in a comparison with different laser power/velocity pairings.

In this (to our knowledge) unique comparison of two different slicers with fs-LDW, the impact of the slicing strategy was examined. Both the slicer from 3DPoli and Cura show individual strengths. This underlines the need to evaluate the slicing strategy individually for each object to be fabricated. Whereas feature sizes were generally lower with Cura, the optical fabrication quality with the 3DPoli slicer was higher. A fast forward way to obtain minimal wall sizes and gap distances is possible with the test artifact. An object fabricated with construction parameters derived from the test artifact further strengthened the point for a common test artifact in fs-LDW.

Furthermore, investigations showed that the degree of curing can be determined on the basis of the Raman signal of the vinyl group and that the presence of oxygen reduces the efficiency of the formation of a network via the vinyl groups. Information of this kind makes it possible to compare writing processes with different parameters and predict the durability and dimensional stability of structures for micro-optical and micro-mechanical applications. What happens during light-curing, however, is a further increase in density due to the accompanying shrinkage process. A test structure whose shape changes in daylight has only limited durability and usefulness. However, a simple post-curing with visible light could solve the problem, and this would also make optical and mechanical microstructures more stable.

Further investigation of the post-curing process with light on suitable geometries, with AFM on stiffness and surface adhesion [50], as well as to make measurements of the resonance frequency of beams to determine the bending modulus [51] are advised for a deeper understanding of fs-LDW structures. In contrast to thermal post-curing, the geometric dimensions change only slightly because the structures do not expand before the curing leads to shrinkage.

The discussed limitations of the test artifact show that a modular version with individual features that can be arranged according to the need of the user would be beneficial. With reduced volume and smaller dimensions, fabrication times could be improved and older fs-DLW setups could be better supported. The drawback here is that the user has to consider the aforementioned constraints themselves.

The test artifact we presented in this work is a first of its kind. Similar to the evolution of test artifacts for metal and polymer additive manufacturing techniques our fs-LDW artifact is not matured yet. We are curious for suggestions to improve the artifact further or to see other designs in the future.

ORCID iDs

Sven Fritzsche https://orcid.org/0000-0002-2521-9266
Brian R Pauw https://orcid.org/0000-0002-8605-838X
Heinz Sturm https://orcid.org/0000-0002-8091-4077

References

[1] Baldacchini T (ed) 2019 Three-dimensional microfabrication using two-photon polymerization *Micro and Nano Technologies* 2nd edn (Norwich, CT: William Andrew Publishing)

[2] Zhou X, Hou Y and Lin J 2015 A review on the processing accuracy of two-photon polymerization *AIP Adv.* **5** 030701

[3] Marino A, Tricinci O, Battaglini M, Filippeschi C, Mattoli V, Sinibaldi E and Ciofani G 2018 A 3D real-scale, biomimetic and biohybrid model of the blood-brain barrier fabricated through two-photon lithography *Small* **14** 1702959

[4] Lemma E D, Spagnolo B, De Vittorio M and Pisanello F 2019 Studying cell mechanobiology in 3D: the two-photon lithography approach *Trends Biotechnol.* **37** 358–72

[5] Erben A *et al* 2020 Precision 3D-printed cell scaffolds mimicking native tissue composition and mechanics *Adv. Healthc. Mater.* **9** 2000918

[6] Gissibl T, Thiele S, Herkommer A and Giessen H 2016 Two-photon direct laser writing of ultracompact multi-lens objectives *Nat. Photon.* **10** 554–60

[7] Jonušauskas L, Gailevičius D, Mikoliūnaitė L, Sakalauskas D, Šakirzanovas S, Juodkazis S and Malinauskas M 2017 Optically clear and resilient free-form µ-optics 3D-printed via ultrafast laser lithography *Materials* **10** 12

[8] Gillis W F *et al* 2018 Carbon fiber on polyimide ultra-microelectrodes *J. Neural Eng.* **15** 016010

[9] Di Giacomo R, Krödel S, Maresca B, Benzoni P, Rusconi R, Stocker R and Daraio C 2017 Deployable micro-traps to sequester motile bacteria *Sci. Rep.* **7** 1–8

[10] Nielsen A V, Beauchamp M J, Nordin G P and Woolley A T 2020 3D printed microfluidics *Annu. Rev. Anal. Chem* **13** 45–65

[11] Ströer F, Hering J, Eifler M, Raid I, von Freymann G and Seewig J 2017 Ultrafast 3D high precision print of micro structures for optical instrument calibration procedures *Addit. Manuf.* **18** 22–30

[12] Eifler M, Hering J, Von Freymann G and Seewig J 2018 Calibration sample for arbitrary metrological characteristics of optical topography measuring instruments *Opt. Express* **26** 16609–23

[13] Matei A, Zamfirescu M, Jipa F, Luculescu C, Dinescu M, Buruiana E, Buruiana T, Sima L and Petrescu S 2010 Two photon polymerization of ormosils *AIP Conf. Proc.* **1278** 843–51

[14] Xing J F, Zheng M L and Duan X M 2015 Two-photon polymerization microfabrication of hydrogels: an advanced 3D printing technology for tissue engineering and drug delivery *Chem. Soc. Rev.* **44** 5031–9

[15] Torgersen J, Qin X H, Li Z, Ovsianikov A, Liska R and Stampfl J 2013 Hydrogels for two-photon polymerization: a

toolbox for mimicking the extracellular matrix *Adv. Funct. Mater.* **23** 4542–54

[16] Xiong Z, Poudel A, Narkar A R, Zhang Z, Kunwar P, Henderson J H and Soman P 2022 Femtosecond laser densification of hydrogels to generate customized volume diffractive gratings *ACS Appl. Mater. Interfaces* **14** 29377–85

[17] Sänger J C, Pauw B R, Sturm H and Günster J 2020 First time additively manufactured advanced ceramics by using two-photon polymerization for powder processing *Open Ceram.* **4** 100040

[18] Sänger J C, Pauw B R, Riechers B, Zocca A, Rosalie J, Maaß R, Sturm H and Günster J 2023 Entering a new dimension in powder processing for advanced ceramics shaping *Adv. Mater.* **35** 2208653

[19] Kunwar P, Xiong Z, Zhu Y, Li H, Filip A and Soman P 2019 Hybrid laser printing of 3D, multiscale, multimaterial hydrogel structures *Adv. Opt. Mater.* **7** 1900656

[20] Dudziak M, Topolniak I, Silbernagl D, Altmann K and Sturm H 2021 Long-time behavior of surface properties of microstructures fabricated by multiphoton lithography *Nanomaterials* **11** 3285

[21] Moylan S, Slotwinski J, Cooke A, Jurrens K and Donmez M A 2014 An additive manufacturing test artifact *J. Res. Natl Inst. Stand. Technol.* **119** 429

[22] Taylor H, Garibay E and Wicker R 2021 Toward a common laser powder bed fusion qualification test artifact *Addit. Manuf.* **39** 101803

[23] Lopes A J, Perez M A, Espalin D and Wicker R B 2020 Comparison of ranking models to evaluate desktop 3D printers in a growing market *Addit. Manuf.* **35** 101291

[24] Saha S K, Divin C, Cuadra J A and Panas R M 2017 Effect of proximity of features on the damage threshold during submicron additive manufacturing via two-photon polymerization *J. Micro Nano-Manuf.* **5** 031002

[25] Steenhusen S, Hasselmann S and Domann G 2017 Strategies for rapid and reliable fabrication of microoptical structures using two-photon polymerization *Proc. SPIE* **10115** 101150

[26] Bunea A I, Castillo Iniesta N D, Droumpali A, Wetzel A E, Engay E and Taboryski R 2021 Micro 3D printing by two-photon polymerization: configurations and parameters for the nanoscribe system *Micro* **1** 164–80

[27] Schweiger S, Schulze T, Schlipf S, Reinig P and Schenk H 2022 Characterization of two-photon-polymerization lithography structures via Raman spectroscopy and nanoindentation *J. Opt. Microsyst.* **2** 033501

[28] Bauer J, Guell Izard A, Zhang Y, Baldacchini T and Valdevit L 2019 Programmable mechanical properties of two-photon polymerized materials: from nanowires to bulk *Adv. Mater. Technol.* **4** 1900146

[29] Fritzsche S, Topolniak I, Weise M and Sturm H 2021 Shape deviations of DLW microstructures in dependency of fabrication parameters *J. Micromech. Microeng.* **31** 125002

[30] Baldacchini T, LaFratta C N and Malinauskas M 2020 Metrology and process control *Three-Dimensional Microfabrication Using Two-Photon Polymerization* (Amsterdam: Elsevier) pp 197–228

[31] Moylan S, Cooke A, Donmez M A, Jurrens K, Moylan S and Slotwinski J 2012 *A Review of Test Artifacts for Additive Manufacturing* (available at: https://www.ncbi.nlm.nih.gov/pmc/articles/PMC4487294/)

[32] Byun H S and Lee K H 2003 Design of a new test part for benchmarking the accuracy and surface finish of rapid prototyping processes *Int. Conf. on Computational Science and its Applications* (Berlin: Springer) pp 731–40

[33] Skliutas E, Lebedevaite M, Kabouraki E, Baldacchini T, Ostrauskaite J, Vamvakaki M, Farsari M, Juodkazis S and Malinauskas M 2021 Polymerization mechanisms initiated by spatio-temporally confined light *Nanophotonics* **10** 1211–42

[34] Burmeister F, Steenhusen S, Houbertz R, Zeitner U D, Nolte S and Tünnermann A 2012 Materials and technologies for fabrication of three-dimensional microstructures with sub-100 nm feature sizes by two-photon polymerization *J. Laser Appl.* **24** 042014

[35] Jonušauskas L, Gailevičius D, Rekštytė S, Baldacchini T, Juodkazis S and Malinauskas M 2019 Mesoscale laser 3D printing *Opt. Express* **27** 15205–21

[36] Bogucki A *et al* 2020 Ultra-long-working-distance spectroscopy of single nanostructures with aspherical solid immersion microlenses *Light: Sci. Appl.* **9** 48

[37] van der Burgt J S, Dieleman C D, Johlin E, Geuchies J J, Houtepen A J, Ehrler B and Garnett E C 2021 Integrating sphere Fourier microscopy of highly directional emission *ACS Photon.* **8** 1143–51

[38] ISO 3:1973 1973 Preferred numbers–series of preferred numbers (available at: www.iso.org/standard/3564.html)

[39] Preuß J A, Gehring H, Schmidt R, Jin L, Wendland D, Kern J, Pernice W H P, de Vasconcellos S M and Bratschitsch R 2023 Low-divergence hbn single-photon source with a 3D-printed low-fluorescence elliptical polymer microlens *Nano Lett.* **23** 407–13

[40] Suzuki T, Morikawa J, Hashimoto T, Buividas R, Gervinskas G, Paipulas D, Malinauskas M, Mizeikis V and Juodkazis S 2012 Thermal and optical properties of sol-gel and SU-8 resists *Proc. SPIE* **8249** 93–101

[41] Obi S 2006 Replicated optical microstructures in hybrid polymers: process technology and applications *PhD Thesis* Université de Neuchâtel

[42] Rys J, Steenhusen S, Schumacher C, Cronauer C and Daraio C 2019 Locally addressable material properties in 3D micro-architectures *Extreme Mech. Lett.* **28** 31–6

[43] Visser T and van der Maas J H 1978 Systematic interpretation of raman spectra of organic compounds. III–carbonyl compounds *J. Raman Spectrosc.* **7** 125–9

[44] Ellwood J A 1989 *Raman Band Intensities of Thioethers and Thiols* (London: University of London, Royal Holloway and Bedford New College)

[45] Jonušauskas L, Juodkazis S and Malinauskas M 2018 Optical 3D printing: bridging the gaps in the mesoscale *J. Opt.* **20** 053001

[46] Park S H, Lee S H, Yang D Y, Kong H J and Lee K S 2005 Subregional slicing method to increase three-dimensional nanofabrication efficiency in two-photon polymerization *Appl. Phys. Lett.* **87** 154108

[47] Zheng X, Cheng K, Zhou X, Lin J and Jing X 2018 An adaptive direct slicing method based on tilted voxel of two-photon polymerization *J. Adv. Manuf. Technol.* **96** 521–30

[48] Žukauskas A, Matulaitienė I, Paipulas D, Niaura G, Malinauskas M and Gadonas R 2015 Tuning the refractive index in 3D direct laser writing lithography: towards grin microoptics *Laser Photon. Rev.* **9** 706–12

[49] Hu Q *et al* 2022 The influence of printing parameters on multi-material two-photon polymerisation based micro additive manufacturing *Addit. Manuf.* **51** 102575

[50] Silbernagl D Ghasem Zadeh Khorasani M, Cano Murillo N, Elert A M and Sturm H 2021 Bulk chemical composition contrast from attractive forces in afm force spectroscopy *Beilstein J. Nanotechnol.* **12** 58–71

[51] Fortini R, Meyer-Plath A, Kehren D, Gernert U, Agudo Jácome L and Sturm H 2020 Measurement of flexural rigidity of multi-walled carbon nanotubes by dynamic scanning electron microscopy *Fibers* **8** 31